Birth of a large volcanic edifice offshore Mayotte via lithosphere-scale dyke intrusion

Nathalie Feuillet, Stephan Jorry, Wayne C Crawford, Christine Deplus, Isabelle Thinon, Eric Jacques, Jean Marie Saurel, Anne Lemoine, Fabien Paquet, Claudio Satriano, et al.

▶ **To cite this version:**

Nathalie Feuillet, Stephan Jorry, Wayne C Crawford, Christine Deplus, Isabelle Thinon, et al.. Birth of a large volcanic edifice offshore Mayotte via lithosphere-scale dyke intrusion. Nature Geoscience, 2021, 14 (10), pp.787-795. ⟨10.1038/s41561-021-00809-x⟩. ⟨hal-03409680⟩

HAL Id: hal-03409680

https://hal.science/hal-03409680v1

Submitted on 29 Oct 2021

HAL is a multi-disciplinary open access archive for the deposit and dissemination of scientific research documents, whether they are published or not. The documents may come from teaching and research institutions in France or abroad, or from public or private research centers.

L'archive ouverte pluridisciplinaire **HAL**, est destinée au dépôt et à la diffusion de documents scientifiques de niveau recherche, publiés ou non, émanant des établissements d'enseignement et de recherche français ou étrangers, des laboratoires publics ou privés.

HAL Authorization

Birth of a large volcanic edifice offshore Mayotte via lithosphere-scale dike intrusion

Nathalie Feuillet[1,*], Stephan. Jorry[2], Wayne C. Crawford[1], Christine Deplus[1], Isabelle Thinon[3], Eric Jacques[1], Jean Marie Saurel[1], Anne Lemoine[3], Fabien Paquet[3], Claudio Satriano[1], Chastity Aiken[2], Océane Foix[1], Philippe Kowalski[1], Angèle Laurent[1], Emmanuel Rinnert[2], Cécile Cathalot[2], Jean-Pierre Donval[2], Vivien Guyader[2], Arnaud Gaillot[2], Carla Scalabrin[2], Manuel Moreira[1], Aline Peltier[1], François Beauducel[1,4], Raphaël Grandin[1], Valérie Ballu[5], Romuald Daniel[1], Pascal Pelleau[2], Jérémy Gomez[1], Simon Besançon[1], Louis Geli[2], Pascal Bernard[1], Patrick Bachelery[6], Yves Fouquet[2], Didier Bertil[3], Arnaud Lemarchand[1], Jérome Van der Woerd[7].

1. Université de Paris, Institut de physique du globe de Paris, CNRS, F-75005 Paris, France
2. IFREMER, Unité Géosciences Marines, Technopole La Pointe du Diable, 29280 Plouzané, France
3. Bureau de Recherches Géologiques et Minières - BRGM, DGR/GBS, F-45060 Orléans, France
4. Université Grenoble Alpes, IRD, ISterre
5. LIttoral ENvironnement et Sociétés (LIENSs) UMR7266, Université de La Rochelle - CNRS, 2 rue Olympe de Gouges, 17000 La Rochelle
6. Université Clermont Auvergne, CNRS, IRD, OPGC, Laboratoire Magmas et Volcans, F-63000 Clermont-Ferrand, France,
7. Institut de Physique du Globe de Strasbourg UMR7516 CNRS Université de Strasbourg, 5 rue René Descartes 67000 Strasbourg, France

Volcanic eruptions shape the Earth's surface and provide a window into deep Earth processes. How the primary asthenospheric melts form, pond and ascend through the lithosphere is, however, still poorly understood. Since 10 May 2018, magmatic activity has occurred offshore eastern Mayotte (North Mozambique channel), associated with large surface displacements, very low frequency earthquakes and exceptionally deep earthquake swarms. Here we present geophysical and marine data from the MAYOBS1 cruise, which reveal that by May 2019, this activity formed a 820 m tall, ~5 km³ volcanic edifice on the seafloor. This is the largest active submarine eruption ever documented. Seismic and deformation data indicate that deep (> 55 km depth) magma reservoirs were rapidly drained through dykes that intruded the entire lithosphere, and that pre-existing subvertical faults in the mantle were reactivated beneath an ancient caldera

structure. We locate the new volcanic edifice at the tip of a 50 km-long ridge composed of many other recent edifices and lava flows. This ridge is an extensional feature inside a wide transtensional boundary that transfers strain between the East African and Madagascar rifts. We propose that the massive eruption originated from hot asthenosphere at the base of a thick old damaged lithosphere.

Since May 10 2018, Mayotte Island (Comoros archipelago, Indian Ocean, *Figure 1a*) has experienced a major magmatic event off its eastern coast. This event generated more than 11000 detectable earthquakes (up to Mw 5.9), surface deformation rates of up to 200 mm/year and unusual very low frequency (VLF) earthquakes [1,2,3]. As of May 2021 (the time of writing), Mayotte is still deforming and both VLF events and earthquakes with Mw up to 4 are still being recorded.

Prior to this event, no recent eruption or significant seismic activity was reported around Mayotte [2]. Only two earthquakes were detected within 100 km of the island since 1972 [4] and the most recent volcanic exposure is a 4-6 kyr-old pumice layer sampled in the lagoon surrounding the island [5].

Recent geodynamic reconstructions suggest that the Comoros archipelago was built on ~150 Ma old oceanic lithosphere accreted to accommodate the opening of the Western Somali Basin [6]. The Comorian volcanism may result from partial melting of the base of this old lithosphere in interaction with plume material [7,8,9], possibly super plumes originating from Africa [10,11,12] , and may have been controlled by lithospheric deformation [13] [14]. Subaerial volcanic activity on Mayotte island began 11 My ago [13]. Well-preserved cones, tuff rings and maar craters in the Northeastern part of the island (on Petite Terre and in and around Mamoudzou [15,7] and further offshore [16] *(Figure 1b)* testify to relatively recent (probably

Holocene, [7]) subaerial explosive volcanic activity. Gas emissions on Petite-Terre indicate magma degassing [17].

The discovery of the eruption and the new volcanic edifice

To determine the origin of the seismicity and deformation and to search for any seafloor volcanic activity, we deployed Ocean Bottom Seismometers (OBS) with attached Absolute Pressure Gauges (APG) and acquired high-resolution marine data (bathymetry, seafloor and water column backscatter), rock dredges and CTD (Conductivity-Temperature-Depth)-Rosette during the MAYOBS1 (2-19 May 2019) cruise aboard the R/V Marion Dufresne [18].

A systematic 12 kHz multibeam echosounder survey east of Mayotte, revealed a 820 m tall new volcanic edifice (NVE) 50 km east of Mayotte *(Figure 1)*. The NVE was detected by comparing our data to those acquired during a 2014 survey by the French Naval Hydrographic and Oceanographic Service (SHOM) [19] *(Figure 2a)*. The edifice sits on an area that, in the 2014 seafloor topography, was locally almost flat at around 3300 m below sea level (bsl).

The NVE has grown on the lower insular slope of Mayotte, at the eastern tip of a WNW-ESE trending volcanic ridge (Mayotte ridge) on the submarine flank of Mayotte (*Figure 1*). The NVE and many other volcanic features along the ridge have high acoustic reflectivity compared to the surrounding sediments, indicating recent volcanic activity all along the ridge *(Figure 1c and extended data Figures 1,2,3)*. The ridge is 50 km long, extending from the most recent subaerial cones and maar craters on Grande-Terre and Petite-Terre islands (MPT Volcanic zone) to the NVE *(Figure 1b)*. It is divided into two main segments, one on the upper slope (western) and one on the mid- to lower-slope (eastern). The eastern segment trends N130°E and is made of many constructional features similar to mafic submarine eruption features observed elsewhere [20,21,22]: cones up to 2 km-wide and 500 m-high, probably monogenetic; lava flows with smooth bathymetry, elongated ridges with steep slopes and

varying orientations, which could result from dykes in more sedimented areas *(Figure 1 and extended data Figure 2d,e)*.

The western segment is made of volcanic features having more complex morphologies and emplaced along different directions *(Figure 1b and extended data Figure 2b,c)*. The main features are: i) Two N40°E and N120°E trending sets of high-backscatter cones and lava flows, northeast and southeast of Petite-Terre, respectively. These sets converge toward the onshore maar craters of Petite-Terre and may have been emplaced along pre-existing fractures or faults; ii) a horse-shoe shaped edifice (the Horseshoe) with a 3.5 km wide cone, steep slopes and a large collapse-induced scar. East of the Horseshoe, several smaller cones and volcanic features are aligned E-W, suggesting eruptive fissures. Large lava flows originate from this fissure system. iii) a 4 km-wide circular structure (the Crown), whose rim is crowned by seven 1 km-wide, 100-150m high volcanic cones. Their arrangement suggests typical post-caldera domes [23]. West of the Crown, submarine canyons and slope failure scars terminate at a N-S trending slope break that may be controlled by faulting. The Crown appears to sit inside a larger 10 km wide flat depression, bounded by faults and fissures, which could be the remnant of an ancient caldera collapse.

The NVE is located at the eastern tip of the eastern segment of the Mayotte ridge *(Figures 1b)*. In May 2019, its summit rose to 2580 m bsl. Its central peak resembles a pyramid with steep and smooth slopes *(Figure 2a and extended data Figure 3)*. Radial ridges, up to 300 m thick and extending up to 5 km from the central pyramid, display hummocky morphology similar to that observed along mid-ocean volcanic ridges [24] and active seamounts [22] and probably correspond to coalesced pillow lava mounds [21]. Beyond and in-between the hummocky ridges, flat areas up to 100 m thick, with high backscatter, could indicate channelized lava flows or sheet flows emplaced at high effusion rates [25]. We calculate the volume of material corresponding to the 2014- 2019 seafloor depth difference to be at least

114 5.0 ± 0.3 km^3 *(Figure 2b)*. Popping fragments of very fresh basanitic pillow lavas (SiO2 47
115 wt%, $Na_20 + K_2O$ 7.1 wt%, MgO 5.7 wt% [26]) were dredged on the northeastern flank of the
116 NVE, near its summit (see *Figure 2a* for sample location and *supplementary S1)*. The lavas,
117 similar to other basanites sampled in northern Mayotte [7] are aphyric with rare
118 microphenocrysts of olivine (Fo70) and Ti-magnetite.
119 A ~1900-m high, vertical acoustic plume, rising through the water column from the NVE
120 summit to ~800 m below the sea surface, was imaged several times during the cruise using
121 the ship-borne multibeam echosounder (*Figure 3*, supplementary movie 1). A vertical
122 CTD/rosette cast to 3137m depth above the northern flank of the NVE, 1000m offset from the
123 summit, showed strong geochemical signatures. High volatile concentrations (H_2 = 550nM,
124 CH_4 = 831 nM, CO_2= 34 µM), high turbidity and high total alkalinity values were associated
125 with temperature and pH anomalies (respectively 0.2°C and 1 pH unit) [27] and *Extended data*
126 *Fig. 4*). Such chemical anomalies are characteristic of submarine eruptions and may reflect
127 magma degassing [28], molten lava interaction with seawater [29] or fluid/water discharge from
128 subsurface storage zones in the crust or sedimentary cover [30]. The height and the strong
129 backscatter signature of the acoustic plume suggest that a mixture of solid particles
130 (pyroclastic/hyaloclastic jet [28]) and/or differentiated fluid phases (droplets, hydrate-coated
131 bubbles or free gas [31]) are driven upward through the water column from the NVE summit [32].
132 High turbidity measured at water depths below 2500 m, on the northern flank of the NVE,
133 likely indicates the presence of these particles [33]. Both the multiple observations of the vertical
134 acoustic plume at the summit of the NVE and the high H_2 concentration 1 km away indicate
135 that the eruption was likely on-going in May 2019 [29].
136 In the upper slope zone, 30 km away from the volcano, two, ~1000-m high acoustic plumes
137 were detected above the Horseshoe edifice *(Figure 1 and extended data Figure 5, movie 2)*
138 but no significant changes in seafloor morphology or reflectivity were detected.

The seismicity and VLF events relocated by OBS data

The combined land-OBS network of seismic stations (supplementary Figure S2.1) detected 17000 events between February 25 and May 6, 2019. We manually relocated about 800 of the largest earthquakes onboard (*see method and supplementary S2*). Ninety-four percent of the earthquakes cluster beneath the western segment of the Mayotte ridge, 40 km west of the NVE and 5 to 15 km east of Petite-Terre (swarm 1, *Figure 1*). Almost all of the remaining events form a secondary swarm beneath the northwestern tip of the eastern segment, 30 km from Petite-Terre and 20 km from the NVE (swarm 2, *Figure 1*). A few events are also scattered along the eastern segment. We searched the full OBS-land catalog for events beneath the NVE, but found none. The located earthquakes are all very deep, ranging from 25±5 to 50±5 km. In addition, all P-S arrival delays recorded by an OBS deployed for 48h above the main swarm were greater than 3 seconds, indicating no events less than 20 km depth *(Figure 4, extended data Figure 6b, method and supplementary S2.2)*. The land-OBS catalog does not show any evidence for seismicity migration, but it only represents a two-month "snapshot" of the activity. To extend the observational time window, we relocated 139 earthquakes recorded by the land stations between May 2018 and the first OBS deployment. All the events were beneath the volcanic ridge *(extended data fig. 6a)*. During the first weeks of the crisis, they were mainly located beneath the northwestern tip of the eastern segment, between 30 and 50 km depth, whereas in the last two weeks of June, a few events occurred closer to the NVE and between 30km-depth and the surface.

In addition to the high frequency seismicity, VLF events were recorded by the OBSs wideband hydrophones. Their waveforms are similar to those of the globally detected November 11 2018 event (exponentially decaying monochromatic signals of approximately 2000s duration, with dominant period of ~15 s and polarized Rayleigh waves), suggesting

repeated excitation of the same radiating source. We located 84 VLF events using waveform cross-correlation *(see method and supplementary S2.3)*, all of them are most probably above seismic swarm 1 *(Figures 4 and extended data Figure 6b)*, at a mean depth of 22 ± 15 km.

GNSS data and APG modeling

The GNSS network includes nine stations on Mayotte Island and two far field stations at Diego Suarez and Grande Glorieuse islands. The geometry is not optimal, preventing geodetic inversions for complicated structures or media. We performed Bayesian inversions [34] of the data using a point source in an elastic half-space with two distinct analytical formalisms: an isotropic point source [35] and a point compound dislocation model (pCDM, [36] *see method, supplementary S3 and extended data Figure 7)*. In both cases, the results indicate ~5 km^3 deflation of a deep reservoir (> 30 km). The simplest and most robust model is the deflation of ~ 40 km deep isotropic source below the eastern segment of the Mayotte ridge. An increase in absolute seafloor pressure measured by all APGs on the OBS frames, interpreted as seafloor subsidence, is compatible with these models *(see method, supplementary S3, extended data Figure 7d)*.

Magma reservoirs and chronology of the eruption

Most of our located seismicity and modelled GNSS sources lie in the lithospheric mantle, beneath the ~17 km deep Moho [37]. Volcanic seismicity this deep is rarely documented [38,39], especially in dense swarms during eruptions.

The distribution of the seismicity in the first weeks of the crisis suggests a dyke migration from the mid-slope zone to the NVE, along the eastern segment of the Mayotte ridge. This is also supported by the migration of the largest earthquakes' Centroid Moment Tensor depths [40] towards the surface *(extended data Figures 6c and 8)* and agrees well with [1,2]. The earthquakes show strike-slip focal mechanisms compatible with a least compressive principal

stress orthogonal to the eastern segment of the ridge. Similar stress trends have been observed during dyking events beneath the Izu peninsula in Japan [41] and in Iceland [42] but at much shallower depths, where they were interpreted as seismic shear faulting caused by stress transfer to the surrounding vertical faults in response to dyke opening and propagation.

During the first six weeks of the crisis, the magma migrated 20 km laterally along the eastern segment of the Mayotte ridge, then upward (*Figure 4* and *extended data Figure 8*). The building of the NVE may have begun in July 2018, once the dyke reached close to the surface [2,1] allowing for high magma flow rates and rapid ensuing growth. On the basis of this assumption, we estimate a minimum mean lava flow rate of ~180m^3s^{-1} between the start of the eruption on the seafloor and our survey (~ 11 months). The local stress probably decreased considerably once the magma path to the NVE was opened, as is observed during many eruptions involving dyke propagation [43], which would explain why no earthquakes were detected beneath the NVE during the OBS deployment.

After the dike reached the near surface, seismicity resumed beneath the mid- and upper-slope volcanic zones *(Figure 4 and extended data Figures 6a,b and 8)* and its pattern appears to be constant since September 2018 [2]. This stationary seismicity could be caused by stress perturbation along pre-existing structures and/or fluid (gas, magma or water) motions. The swarm 1 earthquakes cluster beneath the ancient caldera structure inferred from our high-resolution bathymetry (*Figure 1c* and *extended data Figure 6b and 8*). This seismicity could indicate activation of pre-existing subvertical faults [44] above a deep (> 55 km) depleting reservoir (R1,*4*), as has been observed during caldera collapse events [45]: if so, these faults would be much deeper than documented elsewhere. Analog models for collapse of a caldera with a high-roof aspect ratio (thickness/width >> 1) indicate reverse fault motions during an initial downsag stage [46], in agreement with the focal mechanism of the May 14, 2019 Mw4.9 swarm 1 region earthquake (*Figure 4 and extended data Figure 8*) and [1].

The VLF events located above swarm 1 may be generated by the resonance of a fluid-filled (magma, gas or hydrothermal) shallower cavity or a fluid-filled crack, most probably at the base of the crust. The characteristic frequency and duration of these events are very different from VLF events typically observed in volcanic zones e.g. [47]. Simple up-scaling of fluid resonance models [48,49] implies a shallower reservoir size of several kilometres (R3, *Figure 4*). The excitation mechanism could be rapid slip and related strain on faults close to the reservoir, or episodic collapse of a piston at the base of this shallow reservoir [47]. The acoustic plumes emanating from the overlying Horseshoe edifice may result from actively degassing of this shallower reservoir.

Both the distribution of seismicity over time and the surface deformation models suggest the drainage of an exceptionally deep reservoir by a dyke that propagated from the base of the brittle lithosphere to the eastern portion of the Mayotte ridge, possibly intersecting another vertical storage zone below seismic swarm 2 before reaching the surface *(R2, Figure 4 and extended data Figure 8)*. Within the uncertainties the GNSS isotropic model may reflect the drainage of reservoir R2 in the brittle lithosphere. The deeper reservoir (R1) may have slowly recharged from the asthenosphere before reaching tensile failure in May 2018 [50].

Magma roots and paths.

The eastern segment of the Mayotte ridge, along which the dike propagated, has the same orientation as many other volcanic features over a range of scales (Quaternary dykes, volcanic vent alignments, ridges and volcanic rift zones) in the northeastern part of Mayotte Island [15] and in and around the other Comoros islands [13,51] (*Figure 5 and extended data Figure 9*). The left-lateral en-echelon arrangement of these features resembles that of extensional tectonic structures in a context of oblique extension (i.e in segmented and diffuse strike-slip fault systems [52] or highly-oblique rifting (e.g. [53,54,55]). We infer that the Mayotte ridge results from the interplay between volcanism and tectonics. The location and orientation of the volcanic

features may be in part controlled by the pre-existing Mesozoic fracture zones [6] but they probably also emplace along new tectonic structures. These tectonic structures are extensional (fissures or step-overs) and open as a result of volcano-tectonic interactions in a wide E-W striking zone, to transfer the strain between the N-S striking offshore branches of the East African rift [56] and the grabens of Madagascar (Aloatra and Ankai) [57]. In this context, high strain rates [54] or highly damaged zones may develop [58] (*Figure 5a inset*) in between the main en-echelon extensional structures. Such zones may constitute high-permeability zones where large magmatic reservoirs can develop. The main Comoros volcanic islands may have grown above such zones.

Between Mayotte and Madagascar, the lithosphere-asthenosphere boundary (LAB) is a sharp limit between a high-velocity 150 Ma lithosphere and a low-velocity asthenosphere, at about 70 km depth [59,60]. The low-velocity asthenosphere is interpreted as hot material spreading beneath the Mascarene basin and beyond [61]. Heating of the base of the oceanic lithosphere damaged by extensional tectonic and loaded by Mayotte island [62] may favour the ponding of large volumes of buoyant melts. Pore pressure increase in these zones may in turn favour failure of deep reservoirs and faults inside the brittle lithosphere

The largest eruption ever documented in submarine domain

The NVE extruded volume (as of May 2019) is 30 to 1000 times larger than that estimated for other deep-sea eruptions [63,25,64,21]. It is difficult to evaluate the dense rock equivalent (DRE) volume [20], but, taking an upper bound of 50% for the DRE factor [65], compatible with the 40% vesicularity of our rock sample [26], the DRE erupted volume could be as large as 2.5 km^3, which is larger than the 1.2 to 1.5 km^3 Havre silicic eruption [66]), previously considered to be the largest documented submarine eruption. It would be 2.5 times larger than the Bardabunga eruption (Iceland's largest eruption of the last two centuries) [43] and only 6 times less than Iceland's 1783-1784 Laki eruption, considered to be one of the largest basaltic eruptions

witnessed by humanity [67]. The volumes and flux of emitted lava during the Mayotte magmatic event are comparable to those observed during eruptions at Earth's largest hot spots (Hawaii, Iceland, [43,68] and one quarter of that emplaced yearly over the entire mid-ocean ridge system (mean estimate from spreading rates over the last 80 Ma [69]). It thus represents a considerable input in terms of CO2 flux [70].

Future scenarios could include a new caldera collapse, submarine eruptions on the upper slope, or onshore eruptions. Large lava flows and cones on the upper slope and onshore Mayotte indicate that this has occurred in the past. Since the discovery of the NVE, an observatory has been established to monitor activity in real time (REVOSIMA [71]) and return cruises continue to follow the evolution of the eruption and edifices.

References

1 Cesca, S. *et al*. Drainage of a deep magma reservoir near Mayotte inferred from seismicity and deformation. *Nat*. *Geosci*. **13**, 87-93, doi:10.1038/s41561-019-0505-5 (2020).

2 Lemoine, A., Bertil, D., Roullé, A. & Briole, P. The volcano-tectonic crisis of 2018 east of Mayotte, Comoros islands. *Geophys*. *J*. *Int*.

3 REVOSIMA, R. d. s. V. e. S. d. M. REVOSIMA (2020), Bulletin n°18 de l'activité sismo-volcanique à Mayotte, du 1 au 31 août, . Report No. 2680-1205, (2020).

4 U.S. Geological Survey. (https://earthquake.usgs.gov/earthquakes/search 2019).

5 Zinke, J., Reijmer, J. & Thomassin, B. Systems tracts sedimentology in the lagoon of Mayotte associated with the Holocene transgression. *Sedimentary Geology* **160**, 57-79 (2003).

6 Phethean, J. J. *et al*. Madagascar's escape from A frica: A high‐resolution plate reconstruction for the W estern S omali B asin and implications for supercontinent dispersal. *Geochemistry, Geophysics, Geosystems* **17**, 5036-5055 (2016).

7 Pelleter, A.-A. *et al*. Melilite-bearing lavas in Mayotte (France): An insight into the mantle source below the Comores. *Lithos* **208-209**, 281-297, doi:10.1016/j.lithos.2014.09.012 (2014).

8 Class, C., Goldstein, S. L., Altherr, R. & Bachèlery, P. The process of plume–lithosphere interactions in the ocean basins—the case of Grande Comore. *Journal of Petrology* **39**, 881-903 (1998).

9 Claude-Ivanaj, C., Bourdon, B. & Allègre, C. J. Ra–Th–Sr isotope systematics in Grande Comore Island: a case study of plume–lithosphere interaction. *Earth and Planetary Science Letters* **164**, 99-117 (1998).

10 Ebinger, C. J. & Sleep, N. Cenozoic magmatism throughout east Africa resulting from impact of a single plume. *Nature* **395**, 788-791 (1998).

11 Reiss, M., Long, M. & Creasy, N. Lowermost mantle anisotropy beneath Africa from differential SKS-SKKS shear-wave splitting. *Journal of Geophysical Research: Solid Earth* **124**, 8540-8564 (2019).

12 Class, C., Goldstein, S. L., Stute, M., Kurz, M. D. & Schlosser, P. Grand Comore Island: A well-constrained "low 3He/4He" mantle plume. *Earth and Planetary Science Letters* **233**, 391-409 (2005).

13 Nougier, J., Cantagrel, J. & Karche, J. The Comores archipelago in the western Indian Ocean: volcanology, geochronology and geodynamic setting. *J. Afr. Earth Sci. (1983)* **5**, 135-145 (1986).

14 Michon, L. in *Active volcanoes of the southwest Indian Ocean* (eds P Bachelery, J-F Lénat, A Di Muro, & L Michon) 233-244 (Springer, 2016).

15 Nehlig, P. *et al*. Report French geological map (1/30 000), sheet Mayotte (1179). Orléans: BRGM, 74 p. . **Geological map by Lacquement F., Nehlig P, Bernard J. (2013).** (2013).

16 Audru, J.-C., Guennoc, P., Thinon, I. & Abellard, O. Bathymay : la structure sous-marine de Mayotte révélée par l'imagerie multifaisceaux. *Comptes Rendus Geoscience* **338**, 1240-1249, doi:10.1016/j.crte.2006.07.010 (2006).

17 Sanjuan, B. *et al*. Estimation du potentiel géothermique de Mayotte : Phase 2 - Étape 2. Investigations géologiques, géochimiques et géophysiques complémentaires, synthèse des résultats. 82 (BRGM, Orléans, France, 2008).

18 Feuillet, N. MAYOBS1 French Oceanographic cruise, RV Marion Dufresne. doi:https://doi.org/10.17600/18001217 (2019).

19 SHOM. (2014).

20 Rubin, K. H. *et al*. Volcanic eruptions in the deep sea. *Oceanography* **25**, 142-157 (2012).

21 Chadwick Jr, W. W. *et al*. Recent eruptions between 2012-2018 discovered at West Mata submarine volcano (NE Lau Basin, SW Pacific) and characterized by new ship, AUV, and ROV data. *Frontiers in Marine Science* **6**, 495 (2019).

22 Clague, D. A. *et al*. Structure of Lō'ihi Seamount, Hawai'i, and Lava Flow Morphology from High-resolution Mapping. *Frontiers in Earth Science* **7**, 58 (2019).

23 Cole, J., Milner, D. & Spinks, K. Calderas and caldera structures: a review. *Earth-Science Reviews* **69**, 1-26 (2005).

24 Yeo, I. A. & Searle, R. High-resolution Remotely Operated Vehicle (ROV) mapping of a slow-spreading ridge: Mid-Atlantic Ridge 45° N. *Geochemistry, Geophysics, Geosystems* **14**, 1693-1702 (2013).

25 Clague, D. A. *et al*. High-resolution AUV mapping and targeted ROV observations of three historical lava flows at Axial Seamount. *Oceanography* **30**, 82-99 (2017).

26 Bachelery, P. *et al*. Petrological and Geochemical Characterization of the Lava from the 2018-2019 Mayotte Eruption: First Results. *AGUFM* **2019**, V52D-06 (2019).

27 Cathalot, C. *et al*. Acoustic and Geochemical Anomalies in the Water Column around the Newly Formed Volcano offshore Mayotte Island. *AGUFM* **2019**, V52D-05 (2019).

28 Resing, J. A. *et al*. Active submarine eruption of boninite in the northeastern Lau Basin. *Nature Geoscience* **4**, 799-806 (2011).

29 Baumberger, T. *et al*. Understanding a submarine eruption through time series hydrothermal plume sampling of dissolved and particulate constituents: W est M ata, 2008–2012. *Geochemistry, Geophysics, Geosystems* **15**, 4631-4650 (2014).

30 Baker, E. T. *et al*. Hydrothermal discharge during submarine eruptions: The importance of detection, response, and new technology. *Oceanography* **25**, 128-141 (2012).

31 Chadwick, W. W. *et al*. Imaging of CO2 bubble plumes above an erupting submarine volcano, NW Rota-1, Mariana Arc. *Geochemistry, Geophysics, Geosystems* **15**, 4325-4342 (2014).

32 Somoza, L. *et al*. Evolution of submarine eruptive activity during the 2011–2012 E l H ierro event as documented by hydroacoustic images and remotely operated vehicle observations. *Geochemistry, Geophysics, Geosystems* **18**, 3109-3137 (2017).

33 Sohn, R. A. *et al*. Explosive volcanism on the ultraslow-spreading Gakkel ridge, Arctic Ocean. *Nature* **453**, 1236-1238 (2008).

34 Tarantola, A. Linearized inversion of seismic reflection data. *Geophysical prospecting* **32**, 998-1015 (1984).

35 Anderson, E. Dynamics of formation of cone-sheets, ring-dikes, and cauldron subsidences: Royal Society of Edinburgh Proceedings, v. 56. (1936).

36 Nikkhoo, M., Walter, T. R., Lundgren, P. R. & Prats-Iraola, P. Compound dislocation models (CDMs) for volcano deformation analyses. *Geophysical Journal International*, ggw427 (2016).

37 Dofal, A., Fontaine, F. R., Michon, L., Barruol, G. & Tkalcic, H. in *AGU Fall Meeting 2018*. (AGU).

38 Merz, D., Caplan-Auerbach, J. & Thurber, C. Seismicity and Velocity Structure of Lō'ihi Submarine Volcano and Southeastern Hawai'i. *Journal of Geophysical Research: Solid Earth* **124**, 11380-11393 (2019).

39 Wolfe, C., Okubo, P. & Shearer, P. Mantle fault zone beneath Kilauea Volcano, Hawaii. *Science* **300**, 478-480, doi:10.1126/science.1082205 (2003).

40 Ekström, G., Nettles, M. & Dziewoński, A. The global CMT project 2004–2010: Centroid-moment tensors for 13,017 earthquakes. *Physics of the Earth and Planetary Interiors* **200**, 1-9 (2012).

41 Toda, S., Stein, R. & Sagiya, T. Evidence from the AD 2000 Izu islands earthquake swarm that stressing rate governs seismicity. *Nature* **419**, 58-61, doi:10.1038/nature00997 (2002).

42 Ágústsdóttir, T. *et al*. Strike-slip faulting during the 2014 Bárðarbunga-Holuhraun dike intrusion, central Iceland. *Geophysical Research Letters* **43**, 1495-1503 (2016).

43 Sigmundsson, F. *et al*. Segmented lateral dyke growth in a rifting event at Bárðarbunga volcanic system, Iceland. *Nature* **517**, 191-195, doi:10.1038/nature14111 (2015).

44 Jacques, E. *et al*. in *AGU* (Online everywhere, 2020).

45 Gudmundsson, M. T. *et al*. Gradual caldera collapse at Bárdarbunga volcano, Iceland, regulated by lateral magma outflow. *Science* **353**, aaf8988 (2016).

46 Roche, O., Druitt, T. & Merle, O. Experimental study of caldera formation. *Journal of Geophysical Research: Solid Earth* **105**, 395-416 (2000).

47 Kumagai, H. *et al*. Very-Long-Period Seismic Signals and Caldera Formation at Miyake Island, Japan. *Science* **293**, 687-690, doi:10.1126/science.1062136 (2001).

48 Fazio, M., Alparone, S., Benson, P. M., Cannata, A. & Vinciguerra, S. Genesis and mechanisms controlling tornillo seismo-volcanic events in volcanic areas. *Scientific reports* **9**, 1-11 (2019).

49 Maeda, Y. & Kumagai, H. A generalized equation for the resonance frequencies of a fluid-filled crack. *Geophysical Journal International* **209**, 192-201 (2017).

50 Sigmundsson, F. *et al*. Unexpected large eruptions from buoyant magma bodies within viscoelastic crust. *Nature Communications* **11**, 1-11 (2020).

51 Famin, V., Michon, L. & Bourhane, A. The Comoros archipelago: a right-lateral transform boundary between the Somalia and Lwandle plates. *Tectonophysics* **789**, 228539 (2020).
52 Armijo, R., Meyer, B., Navarro, S., King, G. & Barka, A. Asymmetric slip partitioning in the Sea of Marmara pull-apart: A clue to propagation processes of the North Anatolian fault? *Terra Nova* **14**, 80-86 (2002).
53 Dauteuil, O. & Brun, J.-P. Oblique rifting in a slow-spreading ridge. *Nature* **361**, 145-148 (1993).
54 Brune, S. Evolution of stress and fault patterns in oblique rift systems: 3-D numerical lithospheric - scale experiments from rift to breakup. *Geochemistry, Geophysics, Geosystems* **15**, 3392-3415 (2014).
55 Pagli, C., Yun, S.-H., Ebinger, C., Keir, D. & Wang, H. Strike-slip tectonics during rift linkage. *Geology* **47**, 31-34 (2019).
56 Franke, D. *et al*. The offshore East African Rift System: Structural framework at the toe of a juvenile rift. *Tectonics* **34**, 2086-2104 (2015).
57 Rufer, D., Preusser, F., Schreurs, G., Gnos, E. & Berger, A. Late Quaternary history of the Vakinankaratra volcanic field (central Madagascar): insights from luminescence dating of phreatomagmatic eruption deposits. *Bulletin of volcanology* **76**, 817 (2014).
58 Peacock, D. & Anderson, M. THE SCALING OF PULL - APARTS AND IMPLICATIONS FOR FLUID FLOW IN AREAS WITH STRIKE-SLIP FAULTS. *Journal of Petroleum Geology* **35**, 389-399 (2012).
59 Pratt, M. J. *et al*. Shear velocity structure of the crust and upper mantle of Madagascar derived from surface wave tomography. *Earth and Planetary Science Letters* **458**, 405-417 (2017).
60 Mazzullo, A. *et al*. Anisotropic Tomography Around La Réunion Island From Rayleigh Waves. *J. Geophys. Res. Solid Earth* **122**, 9132-9148, doi:10.1002/2017JB014354 (2017).
61 Barruol, G. *et al*. Large-scale flow of Indian Ocean asthenosphere driven by Réunion plume. *Nat. Geosci*. **12**, 1043-1049, doi:10.1038/s41561-019-0479-3 (2019).
62 Zhong, S. & Watts, A. Lithospheric deformation induced by loading of the Hawaiian Islands and its implications for mantle rheology. *Journal of Geophysical Research: Solid Earth* **118**, 6025-6048 (2013).
63 Watts, A. B. *et al*. Rapid rates of growth and collapse of Monowai submarine volcano in the Kermadec Arc. *Nature Geosci* **5**, 510-515, doi:10.1038/ngeo1473 (2012).
64 Chadwick Jr, W. W. *et al*. A recent volcanic eruption discovered on the central Mariana back-arc spreading center. *Frontiers in Earth Science* **6**, 172 (2018).
65 Schipper, C. I., White, J. D., Houghton, B., Shimizu, N. & Stewart, R. B. Explosive submarine eruptions driven by volatile-coupled degassing at Lōihi Seamount, Hawaii. *Earth and Planetary Science Letters* **295**, 497-510 (2010).
66 Carey, R. *et al*. The largest deep-ocean silicic volcanic eruption of the past century. *Science advances* **4**, e1701121 (2018).
67 Thordarson, T. & Self, S. The Laki (Skaftár Fires) and Grímsvötn eruptions in 1783-1785 *Bull Volcanol* **55**, 233-263 (1993).
68 Neal, C. *et al*. The 2018 rift eruption and summit collapse of Kīlauea Volcano. *Science* **363**, 367-374 (2019).
69 Cogné, J.-P. & Humler, E. Temporal variation of oceanic spreading and crustal production rates during the last 180 My. *Earth and Planetary Science Letters* **227**, 427-439 (2004).

70 Marty, B. & Tolstikhin, I. N. CO2 fluxes from mid-ocean ridges, arcs and plumes. *Chemical Geology* **145**, 233-248 (1998).
71 REVOSIMA, R. d. s. V. e. S. d. M. Bulletin n°16 de l'activité sismo-volcanique à Mayotte, du 1 au 31 mars 2020. (2020).
72 Debeuf, D. *Étude de l'évolution volcano-structurale et magmatique de Mayotte, Archipel des Comores, océan Indien: approches structurale, pétrographique, géochimique et géochronologique*, (2009).
73 Stamps, D., Saria, E. & Kreemer, C. A Geodetic Strain Rate Model for the East African Rift System. *Sci, Rep,* **8**, 732, doi:10.1038/s41598-017-19097-w (2018).
74 Deville, E. *et al*. Active fault system across the oceanic lithosphere of the Mozambique Channel: implications for the Nubia–Somalia southern plate boundary. *Earth and Planetary Science Letters* **502**, 210-220 (2018).
75 Macgregor, D. History of the development of the East African Rift System: A series of interpreted maps through time. Journal of African Earth Sciences 101, 232-252 (2015).

Correspondence and requests for materials should be addressed to Nathalie Feuillet (feuillet@ipgp.fr)

Author Information

Océane Foix

Present address : Montpellier 2 University, France

Manuel Moreira

Present address: Orleans University, France

Affiliations

Université de Paris, Institut de physique du globe de Paris, CNRS, F-75005 Paris, France

Nathalie Feuillet, Wayne C. Crawford, Christine Deplus, , Eric Jacques, Jean Marie Saurel, Claudio Satriano, Océane Foix, Philippe Kowalski, Angèle Laurent, Manuel Moreira, Aline Peltier, François Beauducel, Raphaël Grandin, , Romuald Daniel, Jérémy Gomez, Simon Besançon, Pascal Bernard, Arnaud Lemarchand

IFREMER, Unité Géosciences Marines, Technopole La Pointe du Diable, 29280 Plouzané, France

Stephan. Jorry, Chastity Aiken, Emmanuel Rinnert, Cécile Cathalot, Jean-Pierre Donval, Vivien Guyader, Arnaud Gaillot, Carla Scalabrin, Pascal Pelleau, Louis Geli, Yves Fouquet,

Bureau de Recherches Géologiques et Minières - BRGM, DGR/GBS, F-45060 Orléans, France
Isabelle Thinon, Anne Lemoine, Fabien Paquet, Didier Bertil

LIttoral ENvironnement et Sociétés (LIENSs) UMR7266, Université de La Rochelle - CNRS, 2 rue Olympe de Gouges, 17000 La Rochelle

Valerie Ballu

Université Clermont Auvergne, CNRS, IRD, OPGC, Laboratoire Magmas et Volcans, F-63000 Clermont-Ferrand, France,

Patrick Bachelery

Institut de Physique du Globe de Strasbourg UMR7516 CNRS Université de Strasbourg, 5 rue René Descartes 67000 Strasbourg, France

Jérôme Van der Woerd

Acknowledgements

We thank captain A. Eyssautier and the officers and the crew of the R/V *Marion Dufresne* (TAAF/IFREMER/LDA), GENAVIR's coordinator, M. Boudou D'hautefeuille, and the shipboard operations engineers. We thank the captain and crew of the M/V *Ylang* (SGTM company). This research was supported by the French Ministries of Environment, Research and Overseas under a research project to N.F. (proposal INSU-CT3 TELLUS SISMAYOTTE 2019). The french national geographic Institute (IGN) provided the Mayotte GNSS data. The la Réunion university (Laboratory of atmosphere and hurricanes) provided data from the

DSUA station in Madagascar (contract INTERREG-5 Indian Ocean 2014-2020 "ReNovRisk-Cyclones").

We thank CNRS/INSU, IPGP, IFREMER, BRGM for additional support under internal funds. We thank our colleagues F. Tronel, A. Roulle, E. Dectot, A. Colombain, C. Doubre, Daniel Sauter, Antony Dofal and Antoine Villié for assistance in the field, previous data acquisition, processing and model development. We thank Olivier Desprez de Gesincourt, L. Testut and T. Tranchant for loan and data processing of the seafloor pressure sensors. We thank the French National Marine Hydrographic and Oceanographic Service (SHOM) for providing us with previous data from the area. We thank G. Barruol for discussions. This is IPGP contribution number XXXX.

Author contributions

NF, SJ, WCC, CD, IT, EJ, JMS, ALe, FP, RD, AG, CA, OF, PK, ALa, JPD, LG, JG, VG, PP, ER participated on the MAYOBS1 cruise (NF, SJ and WCC as PI), acquired and processed the geophysical and seismological data. CSa, ALa and PB detected and located the VLF events. AP was in charge of the GNSS installation in Glorieuse island and processed and modeled the GNSS data with FB and RG. VB was in charge of the OBSs APGs and processed their data. SB participated in the first OBS deployment on the Ylang vessel with WC and RD. DB, ALM and JVW were responsible for the installation of new seismological and GNSS stations in Mayotte and of data acquisition onshore. JPD, VG, ER, CC performed the geochemical analysis and interpretation of the water column data. CSc and AG processed the EM122 acoustic data. CD and AG performed the depth changes calculation. CSc provided the interpretation of the water column acoustic data. PBa and YF furnished the rocks sample descriptions and petrological analysis. NF, SJ, CD, PBa, YF, IT, FP, JVW, EJ provided the geological interpretation. NF wrote the paper with the contribution of all other authors. P.B.

JMS, EJ, WCC, CSa, PB, ALe, GL, CA, VB, AG, AP, FB, RG, ER, CC, CSc wrote the method section and the supplementary material.

Competing interests

The authors declare no competing interests.

FIGURE CAPTIONS

Figure 1: The volcanic ridge offshore Mayotte. a) 3D Westward view of Mayotte island and insular slope (vertical exaggeration 3). Green stars: Acoustically-detected plumes above the Horseshoe, the NVE and the degassing area on Petite-Terre island. Left inset: geographic setting and Global Navigation Satellite System (GNSS) surface horizontal displacements stations. Black points: seismic stations. Dashed grey lines: Mesozoic fracture zones [6]. b) Geological interpretations of MAYOBS1 data. Purple patches: Volcanic structures (mainly cones). Pink patches: lava flows and elongated features. Yellow patches: upper slope's high reflective lava flows. NVE: in red (central part) and orange (radial ridges and flat flows). Green stars as in a). Red lines: fissures and faults, dashed lines: inferred faults. black dots: bathymetric depression. White boxes: location of Fig.2a and Extended data Fig. 3. Inset, as in b with MAYOBS backscatter data. Pink dots: Ocean Bottom seismometer (OBS) seismicity: yellow diamonds: location of the Very Low Frequency earthquakes. White boxes: location of extended data Figure 3.

Figure 2: The new volcanic edifice (NVE) offshore Mayotte. a) 30 m resolution bathymetric maps from shipboard EM122 multibeam, illuminated from N290°E. upper panel: SHOM bathymetry collected in 2014 [19]. lower panel: MAYOBS1 bathymetry collected in May 2019 [18]. black circle: position of dredge DR01. b) Depth changes between 2014 and 2019. The change in topography is estimated to be significant when larger than 10 m.

Figure 3: The new volcanic edifice (NVE) and the acoustic plume. a) Southward 3D view of the NVE and the water column acoustic plume observed one hour before the Conductivity-

572 Temperature-Depth (CTD) rosette on May 16th 2019. The White dot and blue patch indicate
573 the position of the CTD rosette deployment, 1 km far from the summit the volcano. Right
574 inset: Processed polar echogram from one EM122 multibeam ping on May 16th (13:33 UT),
575 horizontal and vertical-axes (both in meters) correspond respectively to the cross-track
576 distance and the water depth.
577
578
579
580 **Figure 4: Conceptual model of the submarine eruption offshore Mayotte eruption**.
581 Bathymetry as in Figure 1b, no vertical exaggeration. Purple zones: N130°E volcano-tectonic
582 ridges and segments. Dashed white lines: inferred ancient caldera with degassing zones
583 above. Cross-section: red and reddish zones: magma storage zones (mush or magma
584 chambers) and magma pathways involved in the 2018-2020 Mayotte volcanic crisis and
585 seafloor eruption. Yellow layer: sediments. Dashed lines: subvertical faults beneath inferred
586 caldera possibly reactivated by the deflation of a deep reservoir. White arrow: possible
587 downsag at an initial stage of caldera collapse. Pink dots: 800 earthquakes located using
588 OBSs and land stations. Other dots: 139 earthquakes from before the OBS deployment:
589 colored dots are from the first 6 weeks of the crisis and white dots from the remaining 8
590 months before the OBS deployment. Yellow diamonds: Very Low Frequency (VLF)
591 earthquakes. Blue and red triangles: water and magma movements, respectively. Blue patch:
592 Location, with 3 sigma uncertainties, of the most robust isotropic source deformation model.
593 Moho depth from [37]. Lithosphere/asthenosphere boundary depth from [60,61].
594
595
596 **Figure 5: Regional volcano-tectonic setting of the submarine eruption offshore Mayotte**.
597 a) Volcano-tectonic setting of the new volcanic edifice (NVE). Volcanic cones and ridges
598 (purple) from this study and [13,72,16,51]. Dots and diamonds : earthquakes as in Figure 4 and
599 Extended data Fig. 6 and 8. Focal mechanisms for M>5 earthquakes [40]. Dotted white arrow:
600 dyking intrusion along eastern segment of the Mayotte volcanic ridge. Red ellipse: inferred
601 main volcano-tectonic ridges. Purple ellipses: highly damaged zones in between the en
602 echelon ridges. Thick black arrows: local extension direction. Inset: sandbox model adapted
603 from [58] illustrating the possible arrangement of the main volcano-tectonic structures in
604 Comoros. b) Geodynamic setting of the East African Rift systems. Main tectonic structures
605 and extensional zones in Africa and Madagascar from this study and [73,57,74,75,56]. Purple patches:

Quaternary volcanism in Madagascar [57]. Red dots: M> 2.5 earthquakes [4] with focal mechanisms from [40] for the M>5 earthquakes. Arrows: GNSS horizontal motions [73]. Small purple ellipses in the Comoros as in a) with double dark red arrows: the volcanic ridge east of Mayotte and extension direction. Inset: Simplified tectonic map of the East African Rift system: Yellow highlights: most active rifts and graben; Red ellipse: Transfer zone of the Comoros with direction of lateral motion.

METHODS

Summary

Ship-borne Multibeam data was acquired using a Kongsberg EM122 1°x1° during the 2014 [19] and 2019 [18]. **Ship-borne Multibeam data** were processed with the GLOBE software [76] to provide 30-m grid spaced digital terrain models and seafloor backscatter imagery and to calculate depth differences, surface and volumes. The 3D acoustic water column data from the 2019 cruise were processed using SonarScope (@Ifremer) and GLOBE softwares https://doi.org/10.17882/70460 [76]. **Water column measurements:** A CTD-Rosette Seabird 911+ CTD (Conductivity; Temperature; Depth) equipped with an altimeter, an Aanderaa oxygen optode and a Seapoint Turbidity Meter was mounted on a carousel with 16 ®Niskin sampling bottles (8L) to measure and sample throughout the water column. Sub-sampling was performed for onboard analyses (pH, alkalinity and total CO2 by pH electrode and titrator) and for onshore analyses (CH4 analysis by the purge and trap method and H2 and CO2 analysis by the Headspace method). **Seismology:** 800 earthquakes identified from the onshore catalog were selected in descending magnitude order and manually picked onboard. The seismic network used during the two month deployment included OBSs, onshore local and regional stations (up to 500km distance). The events were relocated with NonLinLoc [77] and an hybrid velocity model based on trials with 6 different velocity models, achieving final location accuracies better than 5km. Eighty-four very low frequency (VLF) earthquakes were

detected between February 25 and April 24, 2019, using an amplitude trigger on ocean bottom hydrophones recordings, filtered between 0.05 and 0.10 Hz, followed by a selection of events with a clear peak frequency and a final visual inspection. VLF earthquakes were located using spatial 3D back-projection of station-pair cross-correlation functions [78], assuming a constant surface-wave speed of 3.5 km/s. A well-constrained epicentral location was obtained for 81 events. **Geodesy:** We inverted the surface deformation recorded by 6 permanent GNSS (Global Navigation Satellite System) receivers installed in Mayotte, Grande Glorieuse and Madagascar. We used both an isotropic model and a triple volumetric discontinuities (pCDM source) in a homogeneous elastic half-space, isotropic material with Poisson's ratio of 0.25 to model the pressure source in depth. Seafloor pressure data (30s sample interval) were pre-processed using harmonic analysis to remove the tides and low-pass filtering to remove residual oscillations interpreted as internal waves.

Water Column: Bathymetry and water column acoustic data.

See also Extended Data Figures 1 to 3 and Figure 5

We mapped the submarine slope and basin adjacent to Mayotte and detected and mapped water column anomalies using ship-borne multibeam surveys over an area of 8600 km^2. Bathymetric data were collected in 2014 by the French *Service Hydrographique et Océanographique de la Marine* [19] using the vessel BHO Beautemps Beaupré. The 2019 data [18] were collected using the R/V Marion Dufresne during the MAYOBS1 cruise (May 3rd to 18th). Both vessels are equipped with identical Kongsberg EM122 multibeam echosounders (12 kHz, 1°x1° beam width). Bathymetry and seafloor backscatter data sets were processed using the GLOBE software [76] with identical 30-m cell grids to allow accurate estimates of differences in depth, surfaces and volumes. Water column acoustic data are only available for the 2019 cruise and processing was performed onboard using the SonarScope (@Ifremer) and GLOBE software packages using published methods [79].

Water column: Sampling and chemical analysis

See also Extended Data Figure 4.

Water column sampling and in situ measurements with CTD-Rosette.

Seawater was sampled using IFREMER's CTD-Rosette, consisting of a Seabird 911+ CTD (Conductivity; Temperature; Depth) instrument mounted on a carousel with 16 8-liter ®Niskin sampling bottles. For this cruise, the CTD-Rosette was equipped with an altimeter, an Aanderaa oxygen optode and a Seapoint turbidity meter. Information from the sensors was transmitted in real time, allowing us to adapt the sampling strategy to observed water column anomalies.

The ®Niskin bottles were subsampled for onboard and onshore analyses. For CH_4 analysis, 125mL glass bulbs were used for analysis using the purge and trap method. The bulbs were allowed to overflow by at least two volumes of seawater and particular care was taken to exclude air bubbles to prevent contamination. While filling, sodium azide was added to prevent future microbial activity. For H_2 and CO_2 analysis, 160 mL vials were filled using the Headspace method. The vials, containing some sodium azide, were filled using a silicone tube connected to the ®Niskin bottle. The silicone tube was inserted to the bottom of the vial in order to completely fill the vial from the bottom to the top, displacing all contained air. The tube was then slowly removed, taking care to avoid any air bubble, and the vial was sealed with a PTFE septum using special crimping pliers. The headspace volume of 10 mL of atmospheric air was added using a needle mounted on a syringe.

CH_4 analysis by the purge and trap method at IFREMER laboratories.

Onshore, the Purge and trap method [80] was used. Once in the laboratory, CH_4 was stripped from seawater using Helium carrier gas, trapped on activated charcoal at -80°C and detected

683 and quantified with a flame ionization detector after separation on a packed column.
684 Calibration was performed injecting of a commercial gas standard (CH_4 107.8ppm). The limit
685 of detection is 0.03nmol/L, the precision (based on five replicates from the same rosette
686 bottle) is within ± 2% (confidence level 95%) and the accuracy is 5%. The CH_4 equipment
687 was set up in a portable clean air-conditioned container, allowing one CH_4 analysis every 6
688 min using two extraction kits.
689 ***CO_2 and H_2 analysis*** were performed at IFREMER laboratories by GC/HID following
690 methods described in [81], except that the headspace vial replaced the syringe.
691
692 ***pH, Total Alkalinity and ΣCO_2 measurements onboard.***
693 pH, Total Alkalinity and ΣCO_2 measurements were performed onboard using a Metrohm 848
694 Titrino Plus titrator. The pH electrode was calibrated using commercially available pH
695 buffers. pH was measured as soon as possible after sample recovery and Total Alkalinity and
696 ΣCO_2 were then determined by direct titration with 0.1N hydrochloric acid. Concentrations
697 were compared to a seawater reference for oceanic CO_2 measurements (Batch 178).
698
699
700 ## Seismology data
701 *See also Supplementary information and Extended Data Figures 6 and 8*
702 The 800 earthquakes discussed in this paper were located using recordings from a network of
703 up to 22 seismological stations equipped with sensors of different types, operating during
704 different time slots comprised between February 25th and May 5th 2019: 6 ocean bottom
705 seismometers (OBS) and up to 16 land stations on Mayotte island, on Grande Glorieuse, on
706 Khartala volcano, in Madagascar and in Kenya. Details on station location, type and quality
707 are provided in Supplementary Information Figures S2.1 and S2.2 and Table S2.1.

An earthquake catalog of 2362 events of magnitude 2.0<M<5.4, between February 25th and May 5th, was produced in near real-time by BRGM using land stations [82]. On board, three groups of operators working around the clock manually picked 800 of the events from the OBS, selected in descending magnitude order, using SeisComP3 software [83]. The Hypo71 software [84] was used for preliminary locations and SeisComP3 was used to compute ML and MLv magnitudes, the velocity model was updated to fit the data (see Supplementary S2) then the NonLinLoc (NLL) software [77] was used to relocate the events. Low-frequency events were detected and analysed using the broadband land stations and the broadband hydrophone (HiTech HTI-90U, 30s cut-off frequency) on the OBSs.

Geodesy data

See Supplementary Material and Extended Data Figures 7

We used the GNSS stations from the Centre National d'Etudes Spatiales (MAYG), EXAGONE's TERIA network (BDRL and GAMO), Precision Topo's Lel@ network (KAWE), IPGP (GLOR) and the Université de la Réunion (DSUA). Sea floor pressure data were collected using Seabird SBE37 pressure sensors deployed on the OBS frames. The seawater pump of each instrument was deactivated to avoid induced noise on the seismometer recordings. Although SBE37s are not designed for seafloor geodesy, previous experiments indicate that their pressure gauge can be used to characterize sudden or large-amplitude deformations [85,86].

Data availability statement

The authors declare that most of the data supporting the findings of this study are available within the paper and its supplementary information files. GNSS data are available on the website « http://mayotte.gnss.fr » and can be downloaded on this ftp site ftp://rgpdata.ign.fr/pub/gnss_mayotte/. Ship-borne geophysical data from the MAYOBS1 cruise can be obtained through the French national oceanographic data center SISMER (http://en.data.ifremer.fr/SISMER) but restrictions apply to the availability of these data. The compilations of older bathymetric and topographic data are available on the SHOM Website (http://www.shom.fr). Rock samples are referenced at https://wwz.ifremer.fr/echantillons/Echantillons/Carte#/map and https://campagnes.flotteoceanographique.fr/search. Samples are accessible on site at IFREMER, Plouzané, France.

Map were created using Globe software https://doi.org/10.17882/70460 [76], ArcGIS® software by Esri (https://www.arcgis.com/index.html), Generic Mapping Tools [87], Adobe illustrator ® (https://www.adobe.com/) and MATLAB.

In addition to Mayobs 1 cruise multibeam data (resolution: 30m) [18], Figs. 1, 2, 4, 5 and Extended data Fig. 1, 2, 3, 6, 7, 8, 9 include topographic and bathymetric data from previous compilation [16,88,89,90], the General Bathymetric Chart of the Oceans (https://www.gebco.net) and Global topography from SRTM GL1 (https://catalog.data.gov/dataset/shuttle-radar-topography-mission-srtm-gl1-global-30m). Litto3D Mayotte (https://diffusion.shom.fr/presentation/litto3d-mayot2012.html). Topography and bathymetry of Figure 5b from GeoMapApp (www.geomapapp.org) / CC BY. In Fig 5 and Extended data Figs.6, 8, 9: focal mechanisms for M>5 earthquakes are from [40]. In Figure 5, M> 2.5 earthquakes are from [4]

Code Availability

Ship-borne Multibeam data were processed with the GLOBE software [76]. The 3D acoustic water column data were processed using SonarScope (@Ifremer) and GLOBE softwares https://doi.org/10.17882/70460 [76]. GNSS solutions were computed using the GipsyX/JPL software available at https://gipsy-oasis.jpl.nasa.gov. Deformation source modeling codes (Mogi and Nikkhoo) are available at https://github.com/IPGP/deformations-matlab and data processing has been achieved using the WebObs open-source system available at https://ipgp.github.io/webobs/.

Pressure gauge data were processed with Python [91]. Very Low Frequency Event analysis has been performed using ObsPy [89] NumPy [92] and Matplotlib [93]. Earthquake phase picking was performed with SeisComP3 [94] and initial locations used Hypo71 [84] Final locations were performed with NonLinLoc [77] and results converted back to SeisComP3 using ObsPy [89].

Method References

76 Globe (GLobal Oceanographic Bathymetry Explorer) Software. (2020).

77 Lomax, A., Michelini, A. & Curtis, A. Earthquake location, direct, global-search methods. *Encyclopedia of complexity and system science* **5**, 1-33 (2009).

78 Poiata, N., Satriano, C., Vilotte, J.-P., Bernard, P. & Obara, K. Multiband array detection and location of seismic sources recorded by dense seismic networks. *Geophysical Journal International* **205**, 1548-1573 (2016).

79 Dupré, S. *et al*. Tectonic and sedimentary controls on widespread gas emissions in the Sea of Marmara: Results from systematic, shipborne multibeam echo sounder water column imaging. *Journal of Geophysical Research: Solid Earth* **120**, 2891-2912 (2015).

80 Charlou, J. L., Dmitriev, L., Bougault, H. & Needham, H. D. Hydrothermal CH4 between 12 N and 15 N over the Mid-Atlantic Ridge. *Deep Sea Research Part A. Oceanographic Research Papers* **35**, 121-131 (1988).

81 Donval, J.-P. & Guyader, V. Analysis of hydrogen and methane in seawater by "Headspace" method: Determination at trace level with an automatic headspace sampler. *Talanta* **162**, 408-414 (2017).

82 Bertil.D, Lemoine.A, Colombain.A, Maisonhaute.E & Dectot.G. (BRGM, Orléans, France, 2018).

83 Hanka, W. *et al*. Real-time earthquake monitoring for tsunami warning in the Indian Ocean and beyond. *Natural Hazards & Earth System Sciences* **10** (2010).

84 Lee, W. H. K. & Lahr, J. C. *HYPO71: A computer program for determining hypocenter, magnitude, and first motion pattern of local earthquakes*. (US Department of the Interior, Geological Survey, National Center for …, 1972).

85 Vilaseca, G. *et al*. Oceanographic Signatures and Pressure Monitoring of Seafloor Vertical Deformation in Near-coastal, Shallow Water Areas: A Case Study from Santorini Caldera. *Marine Geodesy* **39**, 401-421 (2016).

86 Fox, C. G. In situ ground deformation measurements from the summit of Axial Volcano during the 1998 volcanic episode. *Geophysical Research Letters* **26**, 3437-3440 (1999).

87 Wessel, P. & Smith, W. H. New, improved version of Generic Mapping Tools released. *Eos, Transactions American Geophysical Union* **79**, 579-579 (1998).

88 SHOM. (MNT_MAY100m_HOMONIM_WGS84, 2016).

89 Krischer, L. *et al*. ObsPy: A bridge for seismology into the scientific Python ecosystem. *Computational Science & Discovery* **8**, 014003 (2015).

90 JORRY, S. (2014).

91 Van Rossum, G. & Drake, F. L. *Python reference manual*. (iUniverse Indiana, 2000).

92 Harris, C. R. *et al*. Array programming with NumPy. *Nature* **585**, 357-362 (2020).

93 Hunter, J. D. Matplotlib: A 2D graphics environment. *IEEE Annals of the History of Computing* **9**, 90-95 (2007).

94 Weber, B. *et al*. in *Geophysical Research Abstracts*.

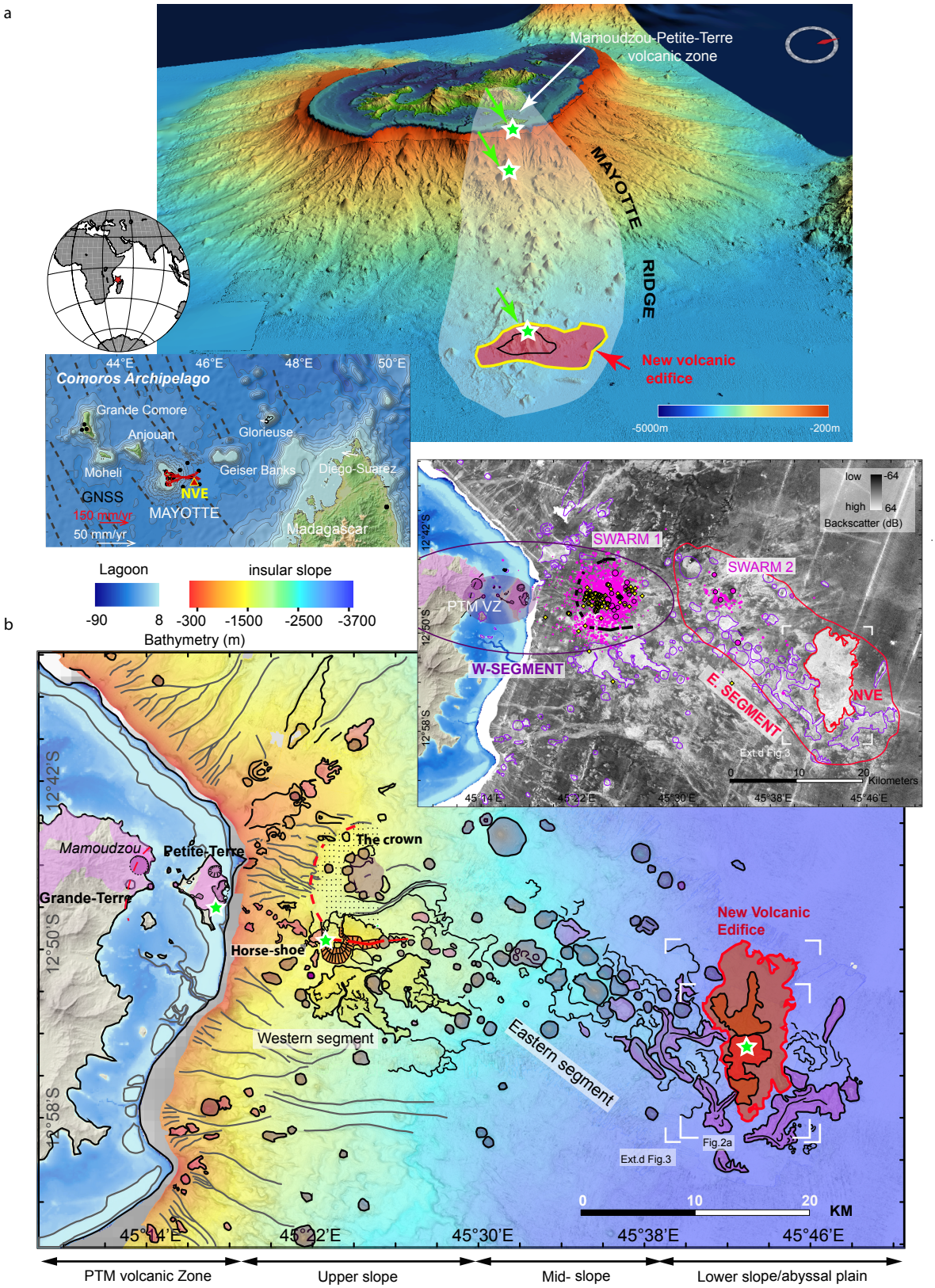
a
Mamoudzou-Petite-Terre
volcanic zone
MAYOTTE
RIDGE
New volcanic
edifice
-5000m
-200m
44°E
46°E
48°E
50°E
Comoros Archipelago
Grande Comore
Anjouan
Moheli
Glorieuse
Geiser Banks
Diego-Suarez
NVE
GNSS
150 mm/yr
50 mm/yr
MAYOTTE
Madagascar
Lagoon
insular slope
-90
8
-300
-1500
-2500
-3700
Bathymetry (m)
b
SWARM 1
SWARM 2
PTM VZ
W-SEGMENT
E. SEGMENT
NVE
low
high
-64
64
Backscatter (dB)
Ext.d Fig.3
0
10
20
Kilometers
12°42'S
12°50'S
12°58'S
45°14'E
45°22'E
45°30'E
45°38'E
45°46'E
Mamoudzou
Petite-Terre
Grande-Terre
The crown
Horse-shoe
Western segment
Eastern segment
New Volcanic
Edifice
Fig.2a
Ext.d Fig.3
0
10
20
KM
PTM volcanic Zone
Upper slope
Mid- slope
Lower slope/abyssal plain

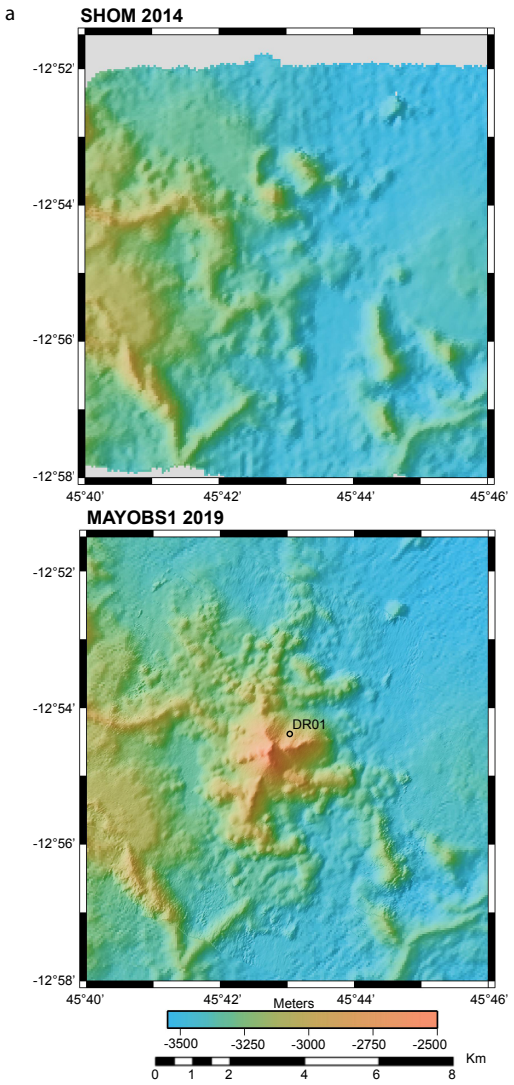
a
SHOM 2014
-12°52'
-12°54'
-12°56'
-12°58'
45°40'
45°42'
45°44'
45°46'
MAYOBS1 2019
DR01
Meters
-3500
-3250
-3000
-2750
-2500
Km
0
1
2
4
6
8

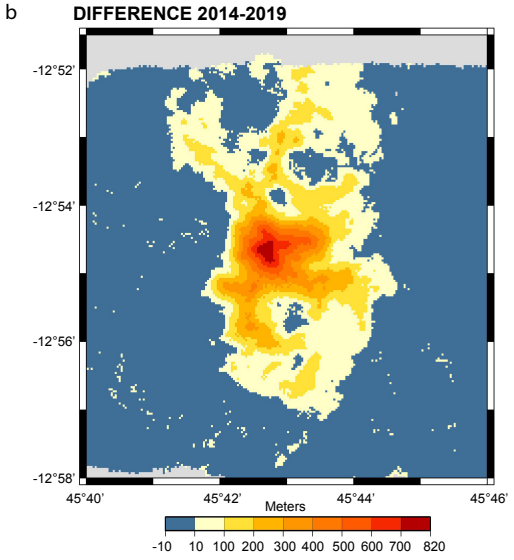
b
DIFFERENCE 2014-2019
-12°52'
-12°54'
-12°56'
-12°58'
45°40'
45°42'
45°44'
45°46'
Meters
-10
10
100
200
300
400
500
600
700
820

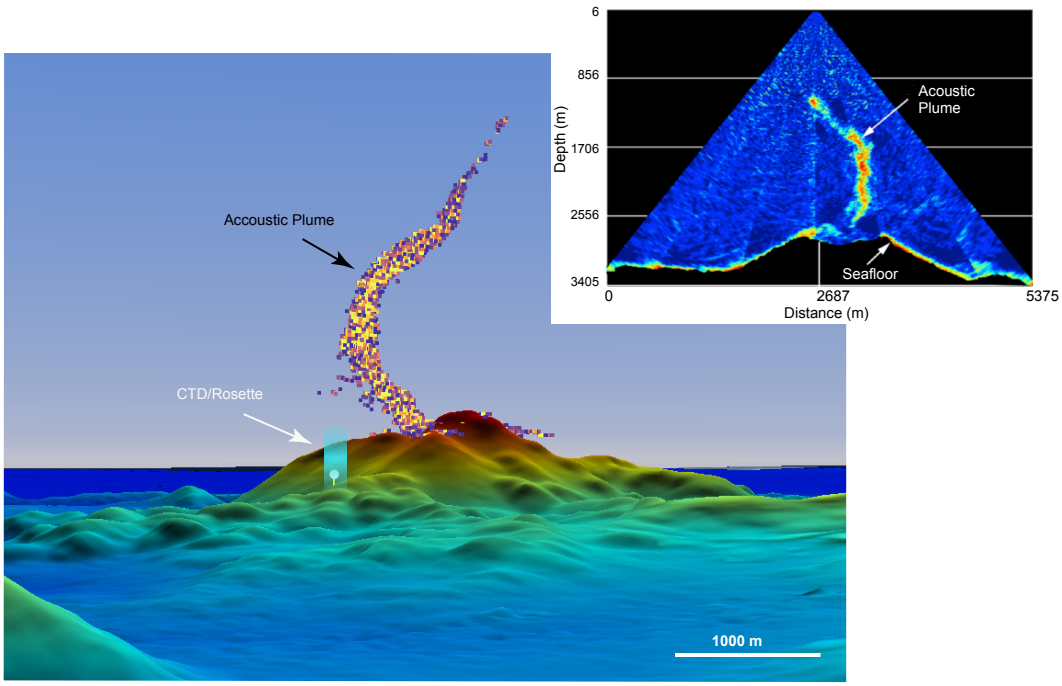
Accoustic Plume
CTD/Rosette
1000 m
6
856
1706
2556
3405
Depth (m)
Acoustic Plume
Seafloor
0
2687
5375
Distance (m)

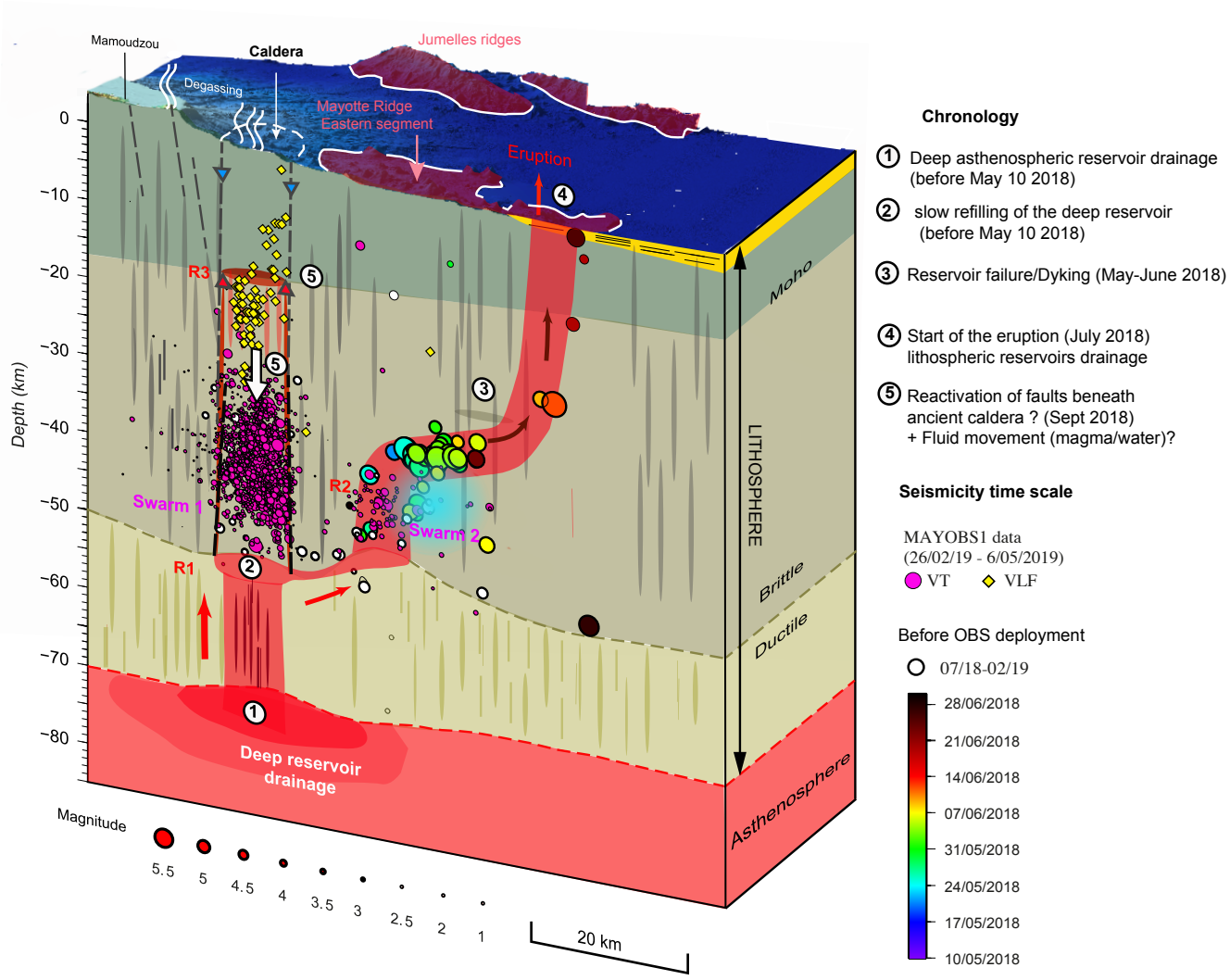
Mamoudzou
Caldera
Jumelles ridges
Degassing
Mayotte Ridge
Eastern segment
Eruption
R3
R2
R1
Swarm 1
Swarm 2
Deep reservoir
drainage
Moho
LITHOSPHERE
Brittle
Ductile
Asthenosphere
Depth (km)
0
-10
-20
-30
-40
-50
-60
-70
-80
Magnitude
5.5
5
4.5
4
3.5
3
2.5
2
1
20 km
Chronology
1 Deep asthenospheric reservoir drainage (before May 10 2018)
2 slow refilling of the deep reservoir (before May 10 2018)
3 Reservoir failure/Dyking (May-June 2018)
4 Start of the eruption (July 2018) lithospheric reservoirs drainage
5 Reactivation of faults beneath ancient caldera ? (Sept 2018) + Fluid movement (magma/water)?
Seismicity time scale
MAYOBS1 data
(26/02/19 - 6/05/2019)
VT
VLF
Before OBS deployment
07/18-02/19
28/06/2018
21/06/2018
14/06/2018
07/06/2018
31/05/2018
24/05/2018
17/05/2018
10/05/2018

a

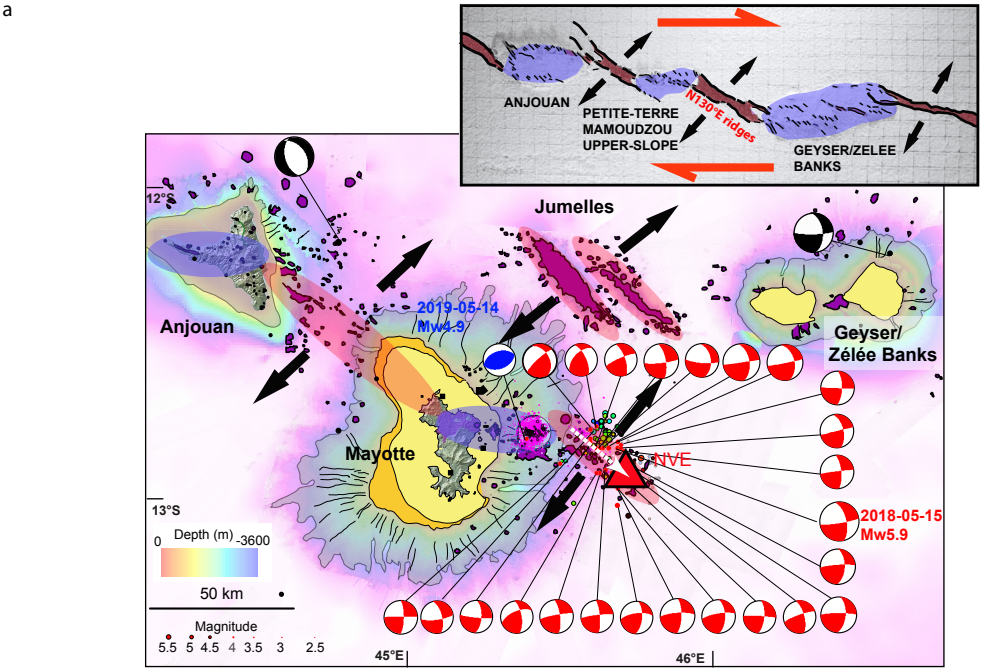
ANJOUAN
PETITE-TERRE
MAMOUDZOU
UPPER-SLOPE
N130°E ridges
GEYSER/ZELEE
BANKS
Jumelles
Anjouan
2019-05-14
Mw4.9
Geyser/
Zélée Banks
Mayotte
NVE
2018-05-15
Mw5.9
12°S
13°S
Depth (m)
0
-3600
50 km
Magnitude
5.5 5 4.5 4 3.5 3 2.5
45°E
46°E

b

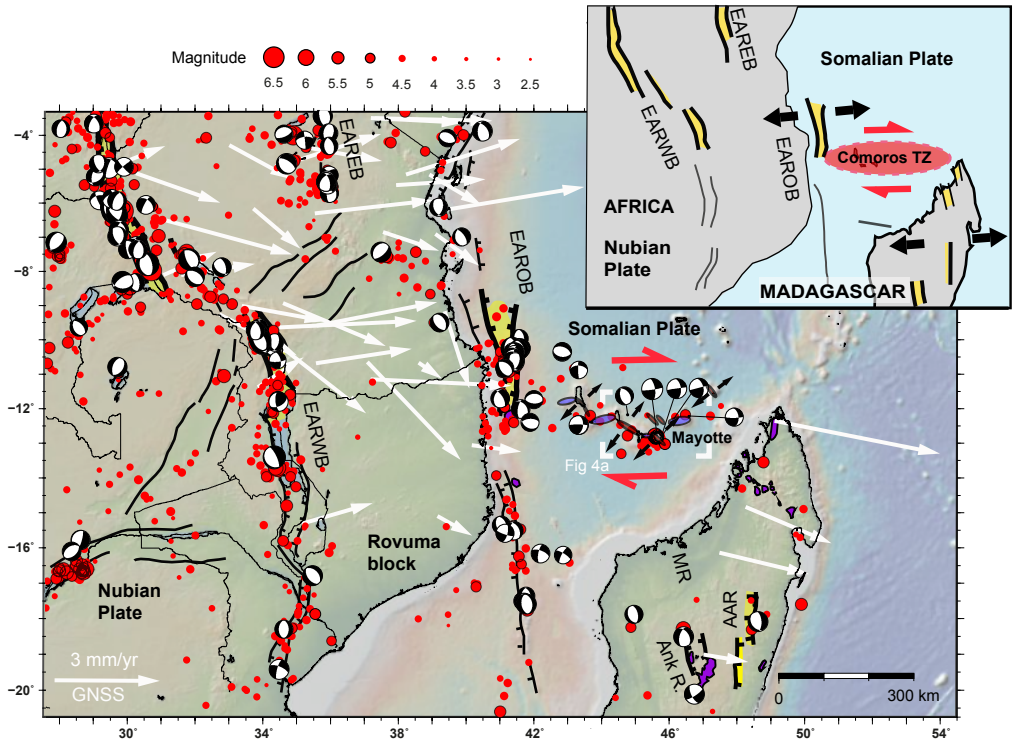
Magnitude
6.5 6 5.5 5 4.5 4 3.5 3 2.5
EAREB
EARWB
EAROB
Somalian Plate
Comoros TZ
AFRICA
Nubian
Plate
MADAGASCAR
Somalian Plate
Mayotte
Fig 4a
Rovuma
block
Nubian
Plate
3 mm/yr
GNSS
MR
AAR
Ank R.
0
300 km
−4°
−8°
−12°
−16°
−20°
30°
34°
38°
42°
46°
50°
54°